scientific reports

Check for updates

OPEN

Computer vision assisted deep transfer learning model for accurate grading of renal cell carcinoma from kidney histopathology images

Mohammed Alghamdi[1], Jamal Alsamri[2], Khaled Mohamad Almustafa[3], Monir Abdullah[4], Abdulsamad Ebrahim Yahya[5]✉, Ahmad A. Alzahrani[6] & Marwa Obayya[2]

Renal cell carcinomas (RCCs) are the seventh most widespread histological cancer. Around 40% of patients die in RCC due to the disease development. Thus, this tumour is the most lethal malignant urological tumour. The histopathologic classification of RCC is vital for the prognosis, diagnosis, and patient management. Classification and detection of intricate RCC histologic patterns on surgical and biopsy surgery slides under a microscope endures a comprehensively specified, time-consuming task and error-prone for pathologists. A wholly automatic and accurate technique of grading kidney tumours from histopathology images (HIs) is in great demand for recognizing harmful cancers. The correct classification of RCC stage and grade is vital for managing medical management, prognosis, and molecular-based treatments. Many preceding works concentrate on machine learning (ML) and deep learning (DL) methods for the RCC classification. The application of DL to study the histopathological images of kidneys, breasts, etc., and other organs contains several tasks like classification of cancer subtypes and grading. This study presents a Computer Vision Assisted Deep Transfer Learning Model for the Accurate Grading of the RCC (CVDTLM-AGRCC) technique. The CVDTLM-AGRCC technique enables the detection and classification of RCC from kidney histopathology images. Initially, the CVDTLM-AGRCC technique applies the image pre-processing stage using a Gaussian filter (GF) to prevent and eliminate the noise. Furthermore, the fusion of ShuffeNetV2-1.0-SE and CapsNet models is employed for the feature extraction. Moreover, the CVDTLM-AGRCC method uses a hybrid of convolutional neural networks and bidirectional long short-term memory (CNN-BiLSTM) techniques for the RCC classification. Finally, the crayfish optimization algorithm (COA) is used for the hyperparameter tuning of the CNN-BiLSTM method. The efficiency of the CVDTLM-AGRCC approach is examined under the KMC dataset. The comparison study of the CVDTLM-AGRCC approach portrayed a superior accuracy value of 93.89% over existing techniques.

Keywords Transfer learning, Renal cell carcinoma, Histopathology images, Crayfish optimization algorithm, Image pre-processing

A kidney tumour is the main reason for the tumour, and renal cell carcinoma (RCC) is the most prevalent among all kidney tumour patients[1]. Estimates and Statistics show rising novel kidney cancer cases globally, and consequently, there is a vital necessity for a precise and fast cancer recognition method to face the forthcoming

[1]Department of Information Systems, College of Computer Science, King Khalid University, Abha, Saudi Arabia. [2]Department of Biomedical Engineering, College of Engineering, Princess Nourah Bint Abdulrahman University, P.O. Box 84428, 11671 Riyadh, Saudi Arabia. [3]Department of Electrical and Computer Engineering, Gulf University for Science and Technology (GUST), GUST Engineering and Applied Innovation Research Center (GEAR), 32093 Hawally, Kuwait. [4]Department of Computer Science and Artificial Intelligence, College of Computing and Information Technology, University of Bisha, 67714 Bisha, Saudi Arabia. [5]Department of Information Technology, College of Computing and Information Technology, Northern Border University, Arar, Saudi Arabia. [6]Department of Computer Science and Artificial Intelligence, College of Computing, Umm Al-Qura University, Mecca, Saudi Arabia. ✉email: Abdulsamad.qasem@nbu.edu.sa

challenges. Predicting the grade and stage of renal cancer is a significant sign parameter for diagnosing kidney tumours[2]. Stage recognition is more regarding the tumour location, size, and in what way deeply the cancer was infected the near lymph nodes. However, the tumour grades define how uncommon or unusual the tumorous cell's appearance is compared to usual healthy cells in the microscope[3]. By the appropriate awareness of grade and stage, the pathologists perceive an indication of how rapidly it will develop and how extreme it will infect other body parts, and the physician could plan the therapy consequently. The physical gradings of intricate histologic forms of clinical slides is a lengthy job, and it is susceptible to errors and contradictions, so it needs greatly specified pathologists[4]. A wholly automatic and precise way of grading kidney tumours from histopathology images (HIs) is in great demand for classifying harmful cancers. HIs provide significant data for prognosis, diagnosis, and cancer staging and are utilized widely by pathologists in medical practice[5]. With the current accessibility of digital whole-slide images, automatic computerized HI study methods have indicated great potential in diagnosis and the detection of novel biosignatures for tumours[6].

While compared with human observation, digital image analysis has a considerable possibility of enhancing consistency, efficiency, and accuracy. Also, HIs have molecular features, like gene expression signatures and inherited changes, that are extensively implemented for predicting experimental cancer results[7]. Histological images encompass markers of phenotypic information and disease development, which could have predictive and diagnostic values. Many pathologists have followed essential decision tree-based techniques for the stratification of tumours. Key boundaries in the inspection of H & E images by pathologists are the time needed to diagnose and inter-observer discordance[8]. Computer-aided techniques could assist in overwhelming these limits and classify restrained morphological variances among the medical groups. Presently, deep learning (DL) and machine learning (ML) systems are extensively considered by researchers[9]. The application of DL to study the HIs of the prostate, liver, breast, kidney, colon, and other organs contains several tasks like nuclei characterization and detection, segmentation of tumour subtypes, and grading. Some current workings use convolutional neural networks (CNN) and the importance of kidney tumours and grading[10]. DL is used efficiently to distinguish kidney HIs into five classes, i.e. Non-tumorous / Normal.

This study presents a Computer Vision Assisted Deep Transfer Learning Model for the Accurate Grading of the RCC (CVDTLM-AGRCC) technique. The CVDTLM-AGRCC technique enables the detection and classification of RCC from kidney histopathology images. Initially, the CVDTLM-AGRCC technique applies the image pre-processing stage using a Gaussian filter (GF) to prevent and eliminate the noise. Furthermore, the fusion of ShuffeNetV2-1.0-SE and CapsNet models is employed for the feature extraction. Moreover, the CVDTLM-AGRCC method uses a hybrid of convolutional neural networks and bidirectional long short-term memory (CNN-BiLSTM) techniques for the RCC classification. Finally, the crayfish optimization algorithm (COA) is used for the hyperparameter tuning of the CNN-BiLSTM method. The efficiency of the CVDTLM-AGRCC approach is examined under the KMC dataset.

- The CVDTLM-AGRCC model applies Gaussian filter (GF)-based image pre-processing to enhance image quality by mitigating noise and preserving key features. This pre-processing step ensures cleaner inputs for model training, improving the system's overall accuracy and reliability. Refining the images directly supports more effective downstream feature extraction and classification tasks.
- The CVDTLM-AGRCC approach integrates ShuffeNetV2-1.0-SE and CapsNet for feature extraction, effectively capturing spatial and contextual data from histopathology images. This fusion improves the model's capability to detect complex patterns and details crucial for accurate cancer grading. Employing both models ensures a comprehensive understanding of the input data, improving classification performance.
- The CVDTLM-AGRCC technique utilizes the hybrid CNN-BiLSTM model, integrating CNN's powerful feature extraction with BiLSTM's capability to capture temporal dependencies, ensuring accurate classification of renal cell carcinomas. This approach improves the method's capability to recognize complex patterns and spatial–temporal relationships in histopathology images. Utilizing both convolutional and sequential learning improves classification performance for cancer grading.
- The CVDTLM-AGRCC methodology implements COA-based hyperparameter tuning to optimize the model's performance by fine-tuning key parameters, resulting in more accurate and efficient results. By utilizing the COA model's search capabilities, the method adapts to intrinsic data patterns. This approach ensures optimal performance across diverse configurations, improving classification accuracy.
- The CVDTLM-AGRCC model introduces a novel hybrid architecture that integrates ShuffeNetV2-1.0-SE, CapsNet, CNN-BiLSTM, and COA. This unique fusion incorporates advanced feature extraction, spatial and contextual learning, and temporal pattern recognition, improving RCC classification accuracy in histopathological images. COA for hyperparameter tuning optimizes the model, giving it superior performance to conventional approaches.

Related works

Yao et al.[11] proposed a fully automatic, strong, and numerically effective RCC Grading Networks (RA***F*** ***2***Nets) technique. This recommended technique combines three various Mobilenet backbones with smart feature fusions. Furthermore, the attention blocks provide significant significance to the pixels, mainly responsible for the classification process. Hao et al.[12] proposed to use whole-slide images examined by light microscopic and immunofluorescence images to categorize cases with membranous nephropathy. The structure primarily contains a confidence coefficient extraction, multimodal fusion, and glomerular segmenting components. This structure initially segments and identifies the glomerulus from immunofluorescence and whole-slide images, and later, a glomerular classification is trained to extract the characteristics of every glomerulus. Abu Haeyeh et al.[13] present a new multiscaled weakly-supervised DL technique for subtyping RCC. This method is initiated using the RGB-histogram requirement colour normalization on the whole-slide images to remove the colour impact differences

from the method execution. Later, the many-instance learning technique is developed by separating the input data into manifold overlapping areas to preserve the connectivity of the tissues. Li et al.[14] proposed to advance and authenticate a DL method. A 2-D TransUNet-based DL method united with the train-while-annotating technique has been trained for renal tumours' automated volumetrical segmentation. PRAT was extracted using a dilatation method by computing VAT voxels adjoining the kidneys. The features of Radiomics are successively extracted from 3 regions of interest in CT images, implementing numerous filtering tactics.

Sun et al.[15] introduced a hybrid multi-case learning method based on the Transformer and the Graph Attention Network, named TGMIL. This technique is separated into three stages. Initially, a feature pyramid with numerous lower intensifications of whole-slide images called MMFP is intended. It creates a method that integrates finer information and decreases the consumption of memory and training time, equating to maximum intensification. Next, TGMIL combines the TGMIL abilities, proficiently tackling the loss of instance spatial and contextual. Mahootiha et al.[16] present a widespread DL method. The structure contains three components: a survival prediction, a clinical variable selection, and a 3D image feature extractor. Medical factors were analytically chosen utilizing the random forest (RF) importance score and Spearman score as standards. Sukegawa et al.[17] proposed classifying the histological classifications from HIs of oral squamous cell carcinoma utilizing CNNs-DL approaches. Oral pathologists organize histopathological models of oral squamous cell carcinoma. Images are separated into covers on an effective label, and slides are used. ResNet50 and VGG16 with the optimizer's gradient stochastic descent with spectral angle mapper (SAM) and momentum are utilized, with and without a learning rate planner. Patel et al.[18] presented an intelligent kidney tumour classification and segmentation method that is executed. The images were provided to the presented 3D-Trans-Residual DenseUnet++ (3D-TR-DUnet++) networks for the segmentation method. A DL-based technique named Adaptable and Attentive Residual Densenet with Gated Recurrent Unit (AA-RD-GRU) has been advanced in categorizing kidney tumours. Duwe et al.[19] developed an AI system that generates evidence-based treatment recommendations for urothelial carcinoma (UC) and RCC by training ML models, such as XGBoost and RF, and utilizing SHapley Additive exPlanations (SHAP) for explainability.

The existing studies concentrate on diverse aspects of RCC classification, such as feature fusion, multimodal image analysis, and DL-based segmentation. However, many of these methods still face difficulty handling the variability in data from diverse sources and the lack of sufficient annotated data for training robust models. Moreover, the computational complexity of models with multimodal and multi-scale approaches may restrict their applicability in real-time clinical environments. Furthermore, while these methods exhibit promise, they often require more advanced data pre-processing and increased memory, making them less effective for massive datasets. There is also a requirement for more generalized techniques that can be applied across diverse cancer types beyond RCC.

Proposed methodology

This work proposes a novel CVDTLM-AGRCC technique. The technique enables the detection and classification of RCC from kidney histopathology images. To accomplish that, the CVDTLM-AGRCC model contains four distinct stages: image pre-processing, fusion of transfer learning, hybrid DL model using classification process, and COA-based parameter tuning. Figure 1 denotes the complete workflow of the CVDTLM-AGRCC model.

Stage I: GF-based image pre-processing

At first, the CVDTLM-AGRCC technique applies the image pre-processing stage using GF to prevent and eliminate noise[20]. This model is chosen because it can effectively mitigate noise while preserving crucial features in histopathology images. This method improves the quality of images before they are passed through complex models, improving their accuracy. Unlike other filtering techniques, GF smooths out high-frequency noise without blurring crucial structural details, making it ideal for medical image analysis. Moreover, its simplicity and computational efficiency make it an ideal choice for massive datasets, ensuring minimal processing time. In the context of renal cell carcinoma classification, GF ensures the extraction of clear, noise-free features, resulting in enhanced model performance and accuracy. Figure 2 illustrates the GF architecture.

GF has been broadly applied in image smoothing. This GF cannot evenly weigh each value within the region, distinct from the mean filter. Instead, the pixels closer to the middle are set at a superior weight further than those more distant. The GF area dimension is defined with zero and Standard Deviation. GF is often selected owing to its distance-dependent weighting and non-sharp transitions. Distance cannot be considered for median and mean filters; they may observe artefacts in an additional, comprehensive image with a higher filter. The GF appearances are precisely revealed below.

Due to the kernel value by a pixel, which is rows r and columns c from the middle is:

$$k_{r,c} = \frac{1}{2\pi\sigma^2}\exp\left(-\frac{r^2+c^2}{2\sigma^2}\right) \tag{1}$$

In practice, GFs are shortened about forty seconds later for values further from the centre; these values are fairly near 0.

Stage II: Fusion of feature extractor

Furthermore, the fusion of the feature extraction process is employed by ShuffeNetV2-1.0-SE and CapsNet models. This fusion technique is chosen due to their complementary strengths. ShuffeNetV2-1.0-SE is known for its effective processing with minimal computational cost, which is particularly beneficial when working with large medical datasets. It utilizes a network shuffle to improve channel interactions, making it an ideal

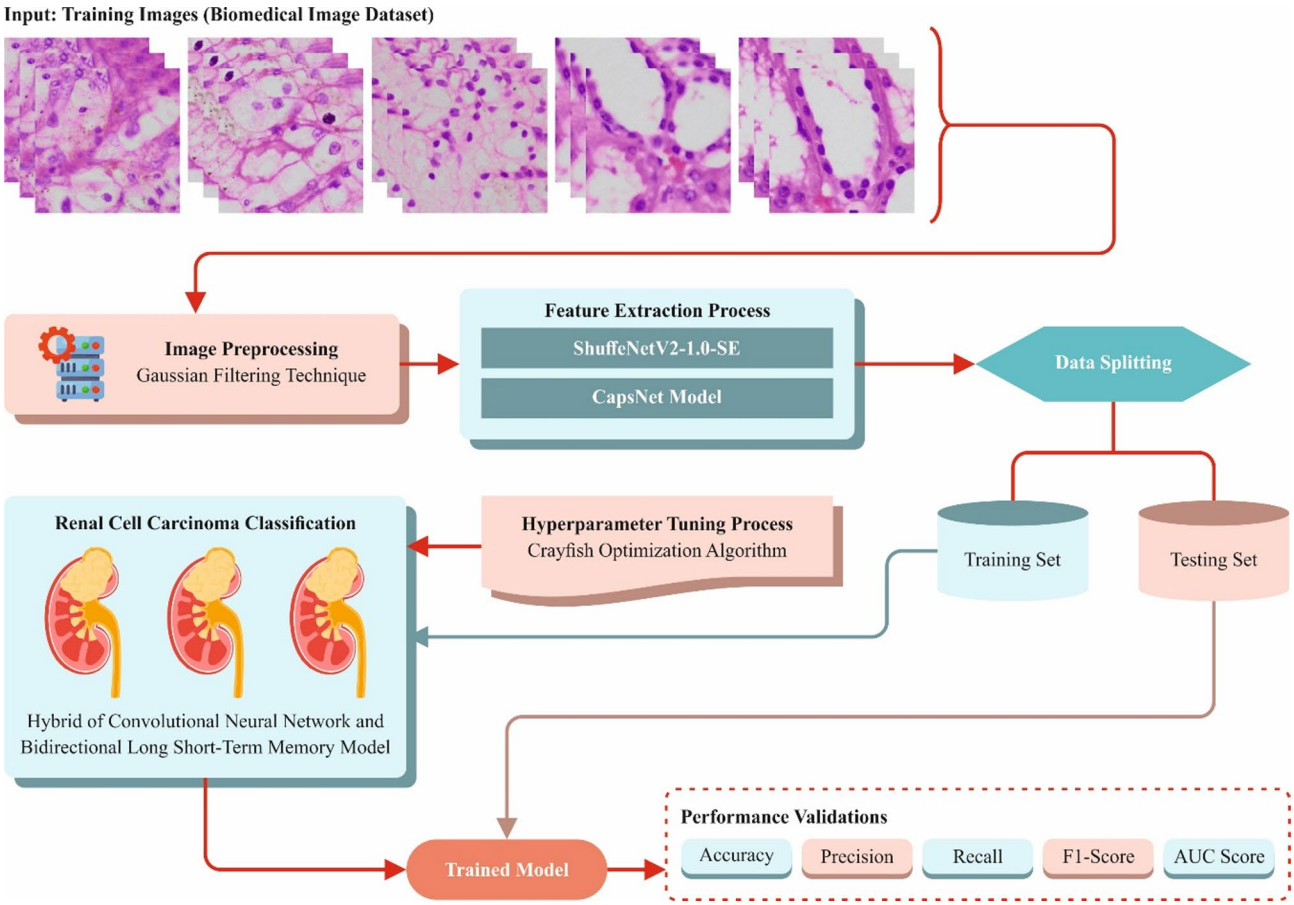

Fig. 1. Overall flow of CVDTLM-AGRCC technique.

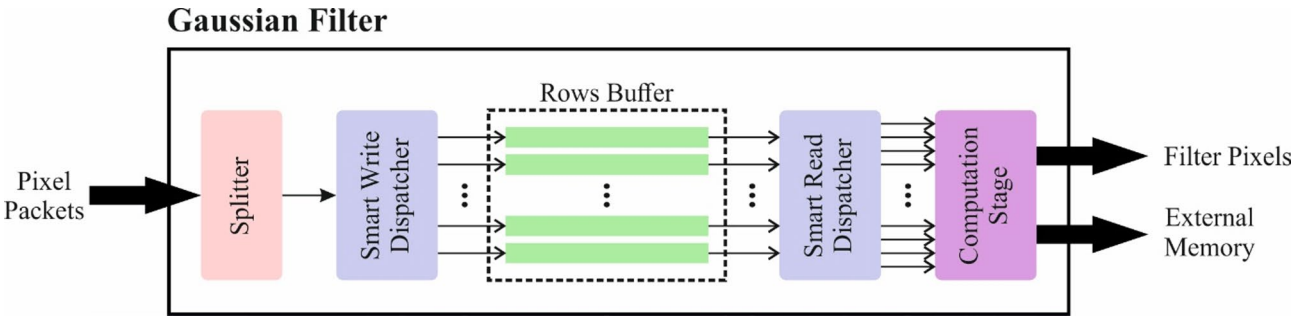

Fig. 2. GF framework.

option for capturing spatial features with mitigated parameter complexity. CapsNet, on the contrary, captures the relationships between features more hierarchically and robustly, which is crucial for comprehending the complex spatial arrangements in histopathology images. By integrating these models, the system benefits from both high efficiency and the capability to model complex patterns, improving the overall performance in detecting subtle cancerous features. This fusion gives a more comprehensive and accurate feature representation than using either model alone.

ShuffeNetV2-1.0-SE model

ShuffeNetV2 utilizes group convolutional for extracting the feature related to ShuffleNetV1[21]. Different depth-wise separable convolutions that use a depth-wise convolutional succeeded by a 1 x 1 point convolutional to tack the outcomes mutually, group convolutional executes only one convolutional and interlinks the outcomes of various groups. It additionally decreases the computing difficulty of the method and upsurges the semantical data interchange among the different groups, which could enhance the feature extraction system's capability. ShuffleNetV2 enhances inter-channel communication and mitigates data loss using a network shuffle technique.

Compared to ShuffleNetV1, ShuffleNetV2 introduces a novel stack block structure consisting of two parts. One part is a standard block repeatedly stacked to form the entire architecture. This design improves the transmission between channel dimensions and adjusts the weight of significant feature channels from input feature maps, U ∈ H x W x C. In contrast, C, H, and W represent the number of channels, width, and height. The module of SE uses a global average pooling (GAP) to decrease the network size to $Z \in 1$ x 1 x C. Later, the part of excitation studies the feature weight of every channel over dual ultimately linked layers and allocates them to dissimilar networks. The ShuffeNetV2-1.0 SE method is recognized by presenting the attention mechanism of SE to the ShuffeNetV2-1.0 structure. The attention mechanism of SE is proposed into the primary fields in the typical block of ShuffeNetV2-1.0 and recognizes the ShuffeNetV2-1.0 SE method structure by stacking. Figure 3 represents the infrastructure of ShuffeNetV2-1.0-SE.

CapsNet model

The Basic CapsNet method input images are rescaled as $75x75$ pixels to decrease the training time[22]. The presented technique holds three disputes: the number of routing iterations, the input image, and the number of classes. Afterwards, input images were pre-processed as in preceding phases and served to the convolutional layer to extract low-level features with filters of 256, the size of the kernel is 9, and strides are 1. Later, these features were clustered into central capsules with filters of $8x32$, kernel of $9x9$, and stride of 1 to decrease the model's size, every one signifying an aspect or part of an object. Every capsule in the convolutional layer resembles a capsule in the key capsule layer. A routing-by-agreement technique is utilized to improve the learning ability and to take the relationship among the various parts of an object. Every capsule in a high-level layer transmits its output to capsules in the layer above based on the deal among their outputs. The routing process iteratively upgrades the connection weights among capsules based on the contest among their outputs.

Hence, dynamic routing creates the capsules in the highest layers with emphasis on the most related capsules in the layer below; the activation function of ReLU is non-linear in DNN, which is utilized to decrease size. The

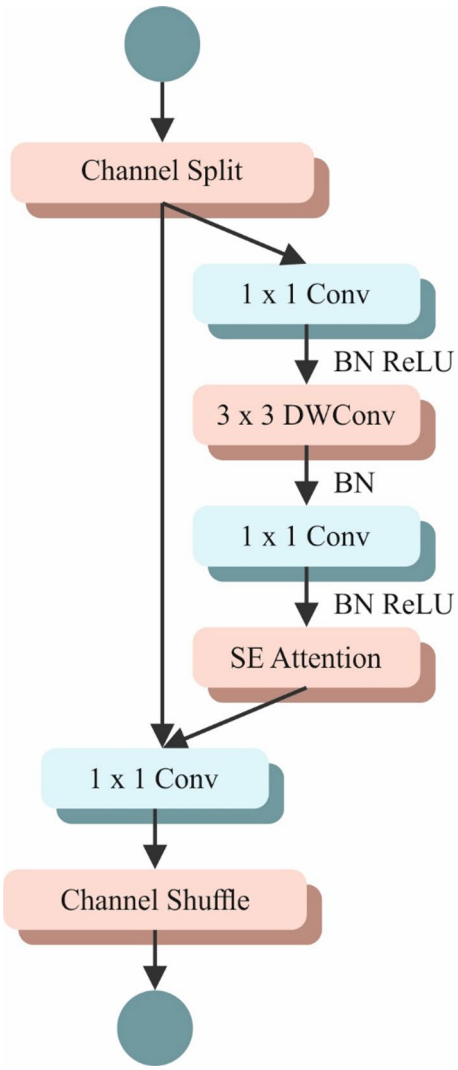

Fig. 3. Structure of ShuffeNetV2-1.0-SE model.

output of the CapsNet is attained by computing the output vector length of the capsules in the topmost layer. This length denotes the possibility that a specified object or class is presented in the input image. Squashing is used for the primary capsule vectors as a non-linear activation function. Its goal was to ensure that the small vectors were decreased to a length close to 0 and that long vectors were decreased to a length close to 1. This study proposes an enhanced CapsNet method, which combines robust pre-trained structures containing GN- CapsNet, VGG16-CapsNet, and RES-CapsNet. This incorporation goals to overwhelm the challenges in classification precision and spatial feature representation utilizing the deep features of these methods.

Stage III: Hybrid of deep learning model

Besides, the CVDTLM-AGRCC method employs a hybrid of the CNN-BiLSTM technique to classify RCC. CNN is extensively utilized in identifying images and other areas as a convolutional (Conv) architecture method in DL systems[23]. CNN could extract comprehensive data attributes efficiently with outstanding implementation. Also, a CNN component is modelled for the time-series predictions of cab travel demands. The component contains batch normalization, a Conv, a pooling, and an activation function layer. In the Conv layer, travel demand local features within the input data were removed by executing Conv processes by the input data utilizing a Conv kernel and sliding window. The batch normalization layer enhances the method's converging speed and strength by implementing the normalization operations on every input data batch. The Exponential Linear Unit (ELU) function is utilized for the activation function, which contains a horizontal activating curve while maintaining the negative data. Lastly, the average pooling extracts the most essential characteristics for dimensional reductions. The recognized CNN component can extract higher-level features.

$$h_i = f\left(W \cdot x_i + b\right) \tag{2}$$

whereas h_i represents the ith output feature map location after the Conv operation. f denotes the activation function. x_i signifies the ith input data location value. W means the Conv kernel used to perform the sliding window Conv procedure utilizing the input data. represents the dot product, for example., multiplication of the matrix. b represents the convolution operation bias term that modifies the convolution output counterbalance.

The providing method is affected by the distribution of data in training. A normalization method is used to tackle the difficulties of vanishing gradients due to the activation function dripping zone. Also, this normalization technique improves the model converging speed, as displayed in Eq. (3). The function of ELU, as shown in Eq. (4), denotes the chosen activation function in this study.

$$Z_{LN} = \frac{z - E(z)}{\sqrt{Var(z) + \varepsilon}} \times \alpha + \beta \tag{3}$$

whereas z denotes the Conv operation result. $E(z)$ signifies the mean. $Var(z)$ means the change. ε denotes a smaller extent superior to 0 to stop the divisor from being fixed to 0, which is usually fixed to 10^{-5}. α, β denotes the training parameters.

$$f\left(Z_{LN}\right) = \begin{cases} Z_{LN'} Z_{LN} > 0 \\ \theta \cdot (e^{Z_{LN}} - 1), Z_{LN} \leq 0 \end{cases} \tag{4}$$

whereas θ signifies the negative slope that limits the functional curve slope while it is lesser than or equivalent to 0.

Then, the feature vectors were transmitted to the GAP layer, where the average value was calculated for the data in every output channel. This upsurges the model strength while reducing the parameter's total assistance. It could stop model overfitting and improve the method's converging speed.

The BiLSTM component can take temporal dependency in time series data by presenting an LSTM mechanism and a bidirectional structure. The component contains dual LSTM systems that carry the input series's reverse and forward handling time steps to take widespread contextual information. The LSTM element could understand the discriminatory holding and overlooking of past state data over input, output, and forgetting gates controls to tackle the long-term dependence issues efficiently.

x_i denotes the input on time t. h_t represents the implicit layer output on time t. f_t signifies the forgetting gate. $_{It}$ signifies the input gate. C_t means the memory unit on time t. 0_t represents the output gate. $\otimes$ signifies the component-wise multiplication. $\oplus$ represents the component-wise addition. The forgetting gate identifies what information is combined with the present memory element, while the output gate manages the memory unit output. C_t and the particular computations were displayed in Eq. (5).

$$\begin{cases} f_t = \sigma\left(W_f \cdot [h_{t-1}, x_t] + b_f\right) \\ i_t = \sigma\left(W_i \cdot [h_{t-1}, x_t] + b_i\right) \\ C_t = \tanh\left(W_c \cdot [h_{t-1}, x_t] + b_c\right) \\ C_t = f_t \otimes C_{t-1} \oplus i_t \otimes C_t \\ \mathrm{o}_t = \sigma\left(W_\mathrm{o} \cdot [h_{t-1}, x_t] + b_\mathrm{o}\right) \\ h_t = \mathrm{o}_t \otimes \tanh C_t \end{cases} \tag{5}$$

whereas W_f, Wi, Wc, Wo, and $b_f, bi, b_c, b_\mathrm{o}$ denote the weighted matrix and bias, $\sigma\ and\ tanh$ mean the sigmoid and hyperbolic tangent activation functions.

The LSTM network parameters were trained sequentially, limiting the complete data usage and declining to extract the inherent feature associated with the data within the time series. The BiLSTM system integrates

backwards and forwards LSTMs to resolve such an issue. Either backward or forward, past data features are extracted concurrently, and the centre connections among the data in the present moments are mined along with the data, consequently enhancing the data usage rate and the method's prediction accuracy.

The presented CNN-BiLSTM component integrates the BiLSTM and CNN and initially encompasses completely connected output and dropout layers; the input layer obtains the time sequence data as input in the CNN-BiLSTM component. Then, the layer of CNN is utilized to extract the spatial feature. The Conv layer takes the local spatial forms within the time series data over Conv processes. The batch normalization layer controls the data and reduces the preference among the various time steps. The activation function presents non-linear properties to enhance the model's significant powers. The pooling layer decreases the dimensional and extracts the main features to enhance the method's computing efficacy and robustness. It follows a layer of BiLSTM, whereas the forward LSTM handles the data from the starting location and the backward LSTM in the concluding location. This bi-directional structure enables the component to take the forward and backward dependency in the sequential data, thus enhancing the capability of sequential development. To alleviate overfitting, a dropout layer is combined that arbitrarily forms the output of a neuron's portion to zero, thus decreasing the method's difficulty and increasing its capability to conclude. The technique maps the BiLSTM layer output to the prediction outcomes in the completely associated layer.

Stage IV: COA-based parameter tuning

Lastly, the COA method is employed for the hyperparameter tunings of the CNN-BiLSTM technique[24]. This method is chosen due to its superior performance in handling complex optimization problems. COA replicates the natural behaviour of crayfish to explore the search space effectively, balancing exploration and exploitation. This results in improved convergence to optimal solutions compared to conventional gradient-based methods, which can often get stuck in local minima. Moreover, the capability of the COA model to adaptively adjust the parameters during the optimization process makes it particularly appropriate for fine-tuning DL models such as CNN-BiLSTM. It also needs fewer assumptions about the nature of the issue, making it more flexible and effective across diverse domains. Applying COA significantly improves the model's performance, ensuring optimal parameter settings that enhance accuracy and efficiency. Figure 4 specifies the steps of the COA technique.

The COA is a meta-heuristic optimizer model stimulated by the crayfish behaviours, like their competition, foraging, and cooling actions. These behaviours correspond to the process's foraging, cooling, and competition stages. The stages of foraging and competition represent the improvement phases of the COA; however, the cooling stage illustrates the exploration phase of the model. The COA has been a method that has been developed recently in the last few years. A complete comparative testing of this model and other conventional optimization algorithms is illustrated. These investigations assessed the performance of every technique on numerous benchmark functions compared to their optimization accuracy, convergence stability, and speed. In detail, they calculated the algorithms' efficiency and ability to control various optimization difficulties, such as how they handle multifaceted searching spaces and vagueness. This efficient comparison establishes that the COA surpasses other accuracy, robustness, and convergence approaches, specifically in successfully discovering global bests for composite optimization problems. However, there are certain limitations, prompting the acceptance of diverse approaches to improve the crayfish model for achieving superior optimization performance.

The exploration and development of the COA depend on $temp$ parameters, with $temp$ performing as an arbitrary variable. If the $temp$ is very high, crayfish look for caves to cool. When no other crayfish are inside the cave, they should access it straightly, which relates to the cooling stage of the method. When other crayfish exist inside the cave, competition starts, demonstrating the competition stage of the algorithm. If the $temp$ is adequate, the model moves to the foraging stage. During this foraging stage, crayfish eat food straight or cut it into pieces preceding a meal, based on the food size. During enhancements in $temp$ balancing, the COA can more effectively discover the best fitness value.

Initialization: During multifaceted optimization problems, every crayfish relates to a 1 x $\dim$ matrix, whereas every column signifies a solution. This COA model is initialized by an N solutions candidate generated at random X among the upper and lower limits. In contrast, N denotes the dimension of the population and $\dim$ signifies the size of the problem. The initialization stage is as demonstrated:

$$X = [X_1, X_2, \ldots, X_N] \tag{6}$$

$$X_{i,j} = lb_j + (ub_j - lb_j) \times rand \tag{7}$$

In the abovementioned equation, lb_j and ub_j represent the lower and upper limits of the dimension j, and $rand$ refers to a randomly generated number within the interval [0,1]. Describing Crayfish Foraging Amount and Temperature: Temperature variants disturb crayfish behaviour, stimulating them to arrive in various phases. If the $temp$ surpasses 30 °C, crayfish search for cooling positions to prevent temperature; they start foraging at the proper temp. The crayfish's hunting quantity has been motivated by temp, using the optimum ranging from 30 °C and 25 °C, and 15 °C is the top. Hence, the foraging amount of crayfish is estimated by a standard distribution, imitating the temp influence. The numerical approach for the foraging number of crayfish and the consistent number at various temperatures were exposed in the subsequent equation.

$$temp = rand \times 15 + 20 \tag{8}$$

Now, $temp$ represents the environmental temp where the crayfish are positioned.

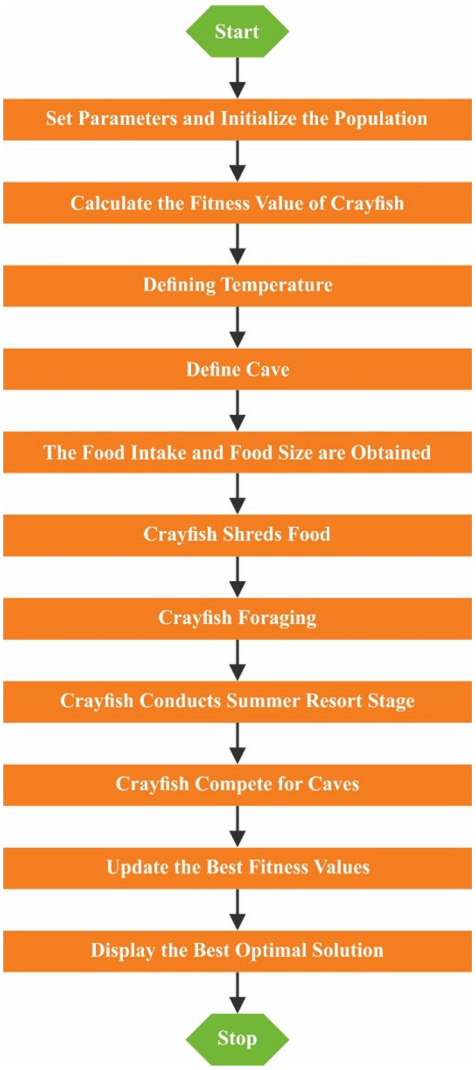

Fig. 4. Steps involved in the COA methodology.

$$p = C_1 \times \left(\frac{1}{\sqrt{2 \times \pi} \times \sigma}\right) \times \exp\left(-\frac{(temp - \mu)^2}{2\sigma^2}\right) \tag{9}$$

where μ means the optimum temperature for the crayfish, however, σ and C_1 are applied to manage the crayfish consumption at various temperatures.

Cooling Phase: If the $temp$ surpasses 30 °C designates that the $temp$ is very high. Now, crayfish will search for caverns to cool off. The description of the cave is demonstrated as follows:

$$X_{shade} = \frac{X_G + X_L}{2} \tag{10}$$

Now, X_{shade} signifies the optimum location gained through the iteration counts, and X_L means the optimum location reached after upgrading the earlier generation population.

The opposition for caverns between crayfish is an arbitrary result. During COA, if $rand < 0.5$, this represents no other crayfish in competition for the cavern. Thus, the crayfish will come straight into the cave to settle down. The equation for crayfish arriving at the cave is as demonstrated:

$$X_{i,j}^{t+1} = X_{i,j}^{t} + C_2 \times rand \times \left(X_{shade} - X_{i,j}^{t}\right) \tag{11}$$

Now, t stands for the present iteration amount, $t + 1$ refers to the following iteration amount, and C_2 represent the declining curve described in the following:

$$C_2 = 2 - \left(\frac{t}{T}\right) \tag{12}$$

where T signifies the maximal iteration counts.

Competition Phase: If the temp goes above 30 °C and $rand \geq 0.5$, this denotes that other crayfish, in addition, select a similar cave. Immediately, they will battle for the cave, and it is described using the subsequent equation:

$$X_{i,j}^{t+1} = X_{i,j}^{t} - X_{z,j}^{t} + X_{shade} \tag{13}$$

$$z = round\,(rand \times (N-1)) + 1 \tag{14}$$

Now, z signifies a randomly formed crayfish individual.

Foraging Phase: If the $temp$ does not exceed 30 °C, it's appropriate for crayfish for foraging. Now, crayfish will begin hunting for nutrition. In foraging, they will determine whether or not to split the food according to its dimensions. If the food size is suitable, the crayfish will eat it straight; when the food is tremendous, they will use their tongs to split it separately and then use their 2nd and 3rd stepping legs to grip and eat the food consecutively. The food description is demonstrated as follows:

$$x_{food} = x_G \tag{15}$$

The food size description is represented as:

$$Q = C_3 \times rand \times \left(\frac{fitness_i}{fitness_{food}}\right) \tag{16}$$

Now, C_3 represents the food aspect denoting the maximal food dimension, with a constant value of three. $Fitness$ signifies the crayfish fitness value i, and $fitness_{food}$ stands for the fitness value by the position of the foods.

If $Q > \frac{C_3+1}{2}$, it illustrates that the food is tremendous. Instantly, the crayfish will utilize the following equation to slit separately the food.

$$x_{food} = \exp\left(-\frac{1}{Q}\right) \times X_{food} \tag{17}$$

When separating the food, the crayfish will use their 2nd and 3rd stepping legs to consume and grasp it. To pretend this interchanging behaviour of serving, a grouping of cosine and sine functions has been applied to model the interchanging method. Furthermore, the amount of food the crayfish gains is also associated with food consumption. The serving Eq. (18) is as established:

$$X_{i,j}^{t+1} = X_{i,j}^{t} + x_{food} \times p \times (\cos(2 \times \pi \times rand) - \sin(2 \times \pi \times rand)) \tag{18}$$

If $\leq \frac{C_3+1}{2}$, the crayfish will travel straightly near the food and eat it. The Eq. (19) is represented as:

$$X_{i,j}^{t+1} = \left(X_{i,j}^{t} - x_{food}\right) \times p + p \times rand \times X_{i,j}^{t} \tag{19}$$

The COA improves a fitness function (FF) to achieve higher classifier performances. It identifies a positive integer to characterize the superior performances of the candidate solutions. In this study, the reduction of the classifier error rate is examined as the FF, as specified in Eq. (20).

$$fitness\,(x_i) = ClassifierErrorRate\,(x_i) = \frac{no.of misclassified samples}{Total no.of samples} \times 100 \tag{20}$$

Experimental validation

The comparative study of the CVDTLM-AGRCC approach is examined under the KMC dataset[25]. The suggested technique is simulated by employing Python 3.6.5 tool on PC i5-8600 k, 250 GB SSD, GeForce 1050Ti 4 GB, 16 GB RAM, and 1 TB HDD. The parameter settings are provided in the following: learning rate: 0.01, activation: ReLU, epoch count: 50, dropout: 0.5, and batch size: 5. The database consists of 3000 samples under five classes, as displayed in Table 1. Figure 5 denotes the sample images.

Figure 6 demonstrates the confusion matrices the CVDTLM-AGRCC methodology produces below different epoch counts. The findings state that the CVDTLM-AGRCC technique effectively classifies and precisely recognizes all 5 class labels.

Table 2 and Fig. 7 signify the RCC recognition values of the CVDTLM-AGRCC algorithm under various epoch counts. The table values indicate that the CVDTLM-AGRCC methodology appropriately identified all five samples. On 500 epoch counts, the CVDTLM-AGRCC algorithm delivers an average $accu_y$ of 93.33%, $prec_n$ of 83.37%, $reca_l$ of 83.33%, $F1_{score}$ of 83.26%, and AUC_{score} of 89.58%. Also, on 1000 epochs, the CVDTLM-AGRCC system provides an average $accu_y$ of 92.99%, $prec_n$ of 82.47%, $reca_l$ of 82.47%, $F1_{score}$ of 82.40%, and AUC_{score} of 89.04%. Besides, on 2000 epoch counts, the CVDTLM-AGRCC algorithm offers an average $accu_y$ of 93.67%, $prec_n$ of 84.14%, $reca_l$ of 84.17%, $F1_{score}$ of 84.11%, and AUC_{score} of 90.10%. Eventually, on 3000 epochs, the CVDTLM-AGRCC system offers an average $accu_y$ of 93.47%, $prec_n$ of 83.66%, $reca_l$ of 83.67%, $F1_{score}$ of 83.61%, and AUC_{score} of 89.79%.

Class	Class description	No. of images
Grade-0 or Normal	Cells are well arranged and are normal in number	600
Grade-1	Nucleoli are not visible at 400× magnification. Nucleoli are seen as eosinophilic at 400× magnification but not very prominent at 100× magnification	600
Grade-2	Slightly irregular contour compared to normal nuclei	600
Grade-3	Visible tumours were graded as grade-3	600
Grade-4	Rhabdoid or sarcomatoid differentiation	600
Total number of images		3000

Table 1. Details of dataset.

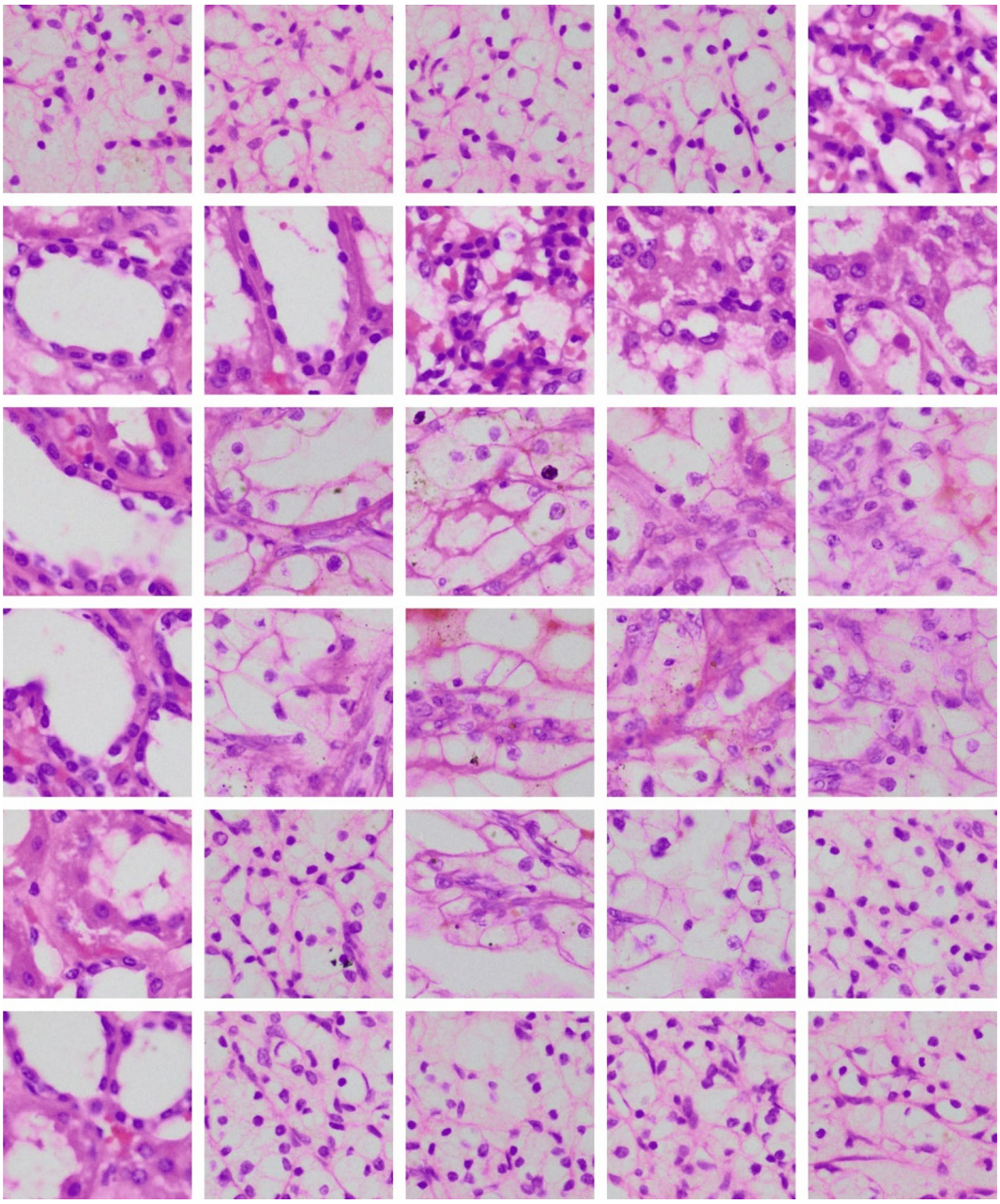

Fig. 5. Sample images.

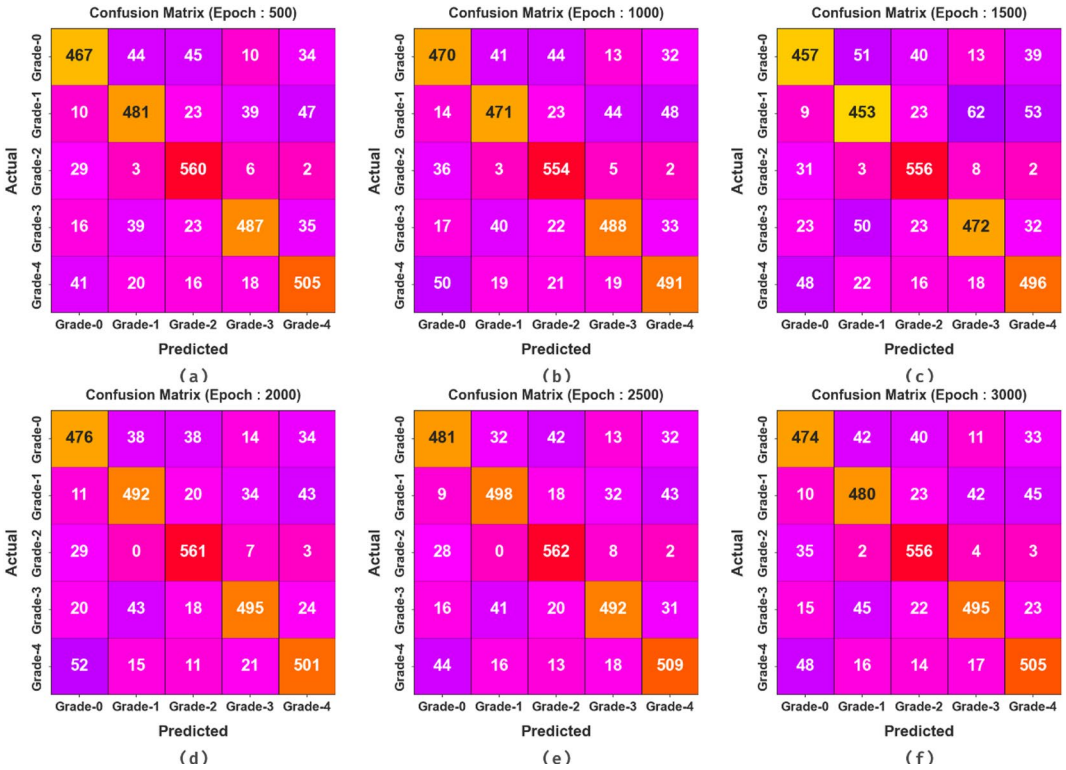

Fig. 6. Confusion matrices of CVDTLM-AGRCC technique (**a**–**f**) Epochs 500–3000.

Figure 8 shows the training $accu_y$(TRAAC) and validation $accu_y$(VLAAC) values of the CVDTLM-AGRCC technique under different epochs. The rate of $accu_y$ is estimated for 0–3000 epoch counts. The figure underlined that the rate of TRAAC and VLAAC displays a growing trend, which indicates the capability of the CVDTLM-AGRCC system to have enhanced execution over various iterations. Moreover, the TRAAC and VLAAC stay nearer over the epochs, which specifies lower minimum overfitting and shows improved performances of the CVDTLM-AGRCC algorithm, promising constant prediction on hidden samples.

Figure 9 shows the TRA loss (TRALS) and VLA loss (VLALS) graph of the CVDTLM-AGRCC system under different epochs. The rate of loss is estimated for 0–3000 epochs. It is denoted that the rate of TRALS and VLALS show a decreasing tendency, reporting the capability of the CVDTLM-AGRCC approach to balance a trade-off between generalization and data fitting. The incessant reduction in the loss rate guarantees the more excellent execution of the CVDTLM-AGRCC technique and fine-tuning of the prediction values over time.

In Fig. 10, the precision-recall (PR) curve study of the CVDTLM-AGRCC system under different epochs provides interpretation into its execution by plotting Precision against Recall for all 5 class labels. The figure exhibits that the CVDTLM-AGRCC technique incessantly achieves better PR values across various classes, representing its capability to retain a substantial portion of true positive predictions among every positive prediction (precision) while taking a significant proportion of actual positives (recall). The constant increase in PR values between all 5 class labels represents the efficacy of the CVDTLM-AGRCC algorithm in classification.

Figure 11 analyses the ROC curve of the CVDTLM-AGRCC model under different epochs. The findings denote that the CVDTLM-AGRCC approach attains greater ROC values over every class, representing the critical ability to differentiate the class labels. This consistent tendency of better ROC values over several class labels indicates the efficient performances of the CVDTLM-AGRCC technique in predicting class labels, emphasizing the intense nature of the classification process.

Table 3 and Fig. 12 study the comparative outcome of the CVDTLM-AGRCC model with the current techniques[19,26–28]. The table values underlined that the ShuffleNet, NASNet, and IncResV2 methods have depicted poor performances. Meanwhile, REGNET-400, SE_RESNET-50, and ResNet-18 methods have attained slightly more excellent finding outcomes. At the same time, the DLF-ACHKWI approach has nearer values with $prec_n$, $reca_l$, $accu_y$, and F_{score} of 82.71%, 79.72%, 92.00%, and 78.73%, respectively. Furthermore, the XGBoost, RF, and SHAP methods illustrated lesser values. The presented CVDTLM-AGRCC methodology exhibited improved performances with maximal $prec_n$, $reca_l$, $accu_y$, and F_{score} of 84.75%, 84.73%, 93.89%, and 84.68%, respectively.

In Table 4 and Fig. 13, the comparative outcome of the CVDTLM-AGRCC algorithm is stated for execution time (ET). The result implies that the CVDTLM-AGRCC system acquires superior execution. In terms of ET, the CVDTLM-AGRCC methodology offers lower ET of 3.18 s while the XGBoost, RF, SHAP, ResNet-18, DLF-ACHKWI, SE_RESNET-50, REGNET-400, IncResV2, NASNet, and ShuffleNet models get better ET values of 5.90 s, 6.11 s, 8.00 s, 9.10 s, 9.89 s, 7.55 s, 5.65 s, 7.41 s, 6.04 s, and 9.31 s, respectively.

Class	$Accu_y$	$Prec_n$	$Reca_l$	$F1_{score}$	AUC_{score}
Epoch-500					
Grade-0	92.37	82.95	77.83	80.31	86.92
Grade-1	92.50	81.94	80.17	81.04	87.87
Grade-2	95.10	83.96	93.33	88.40	94.44
Grade-3	93.80	86.96	81.17	83.97	89.06
Grade-4	92.90	81.06	84.17	82.58	89.62
Average	93.33	83.37	83.33	83.26	89.58
Epoch-1000					
Grade-0	91.77	80.07	78.33	79.19	86.73
Grade-1	92.27	82.06	78.50	80.24	87.10
Grade-2	94.80	83.43	92.33	87.66	93.87
Grade-3	93.57	85.76	81.33	83.49	88.98
Grade-4	92.53	81.02	81.83	81.43	88.52
Average	92.99	82.47	82.47	82.40	89.04
Epoch-1500					
Grade-0	91.53	80.46	76.17	78.25	85.77
Grade-1	90.90	78.24	75.50	76.84	85.13
Grade-2	95.13	84.50	92.67	88.39	94.21
Grade-3	92.37	82.37	78.67	80.48	87.23
Grade-4	92.33	79.74	82.67	81.18	88.71
Average	92.45	81.06	81.13	81.03	88.21
Epoch-2000					
Grade-0	92.13	80.95	79.33	80.13	87.33
Grade-1	93.20	83.67	82.00	82.83	89.00
Grade-2	95.80	86.57	93.50	89.90	94.94
Grade-3	93.97	86.69	82.50	84.54	89.67
Grade-4	93.23	82.81	83.50	83.15	89.58
Average	93.67	84.14	84.17	84.11	90.10
Epoch-2500					
Grade-0	92.80	83.22	80.17	81.66	88.06
Grade-1	93.63	84.84	83.00	83.91	89.65
Grade-2	95.63	85.80	93.67	89.56	94.90
Grade-3	94.03	87.39	82.00	84.61	89.52
Grade-4	93.37	82.50	84.83	83.65	90.17
Average	93.89	84.75	84.73	84.68	90.46
Epoch-3000					
Grade-0	92.20	81.44	79.00	80.20	87.25
Grade-1	92.50	82.05	80.00	81.01	87.81
Grade-2	95.23	84.89	92.67	88.61	94.27
Grade-3	94.03	86.99	82.50	84.69	89.71
Grade-4	93.37	82.92	84.17	83.54	89.92
Average	93.47	83.66	83.67	83.61	89.79

Table 2. RCC detection of CVDTLM-AGRCC technique (a-f) Epochs 500–3000.

Conclusion

In this work, a new CVDTLM-AGRCC technique is proposed. The CVDTLM-AGRCC technique enables the detection and classification of RCC from kidney HIs. To accomplish that, the CVDTLM-AGRCC model comprises four distinct stages: image pre-processing, fusion of transfer learning, hybrid DL model using classification process, and COA-based parameter tuning. At first, the CVDTLM-AGRCC technique applies the image pre-processing stage using GF to prevent and eliminate the noise. Furthermore, the fusion of ShuffeNetV2-1.0-SE and CapsNet models is used for feature extraction. Moreover, the CVDTLM-AGRCC method employs the hybrid CNN-BiLSTM technique to classify RCC. Finally, the COA is implemented for the hyperparameter tuning of the CNN-BiLSTM technique. The efficiency of the CVDTLM-AGRCC approach is examined under the KMC dataset. The comparison study of the CVDTLM-AGRCC approach portrayed a superior accuracy value of 93.89% over existing techniques.

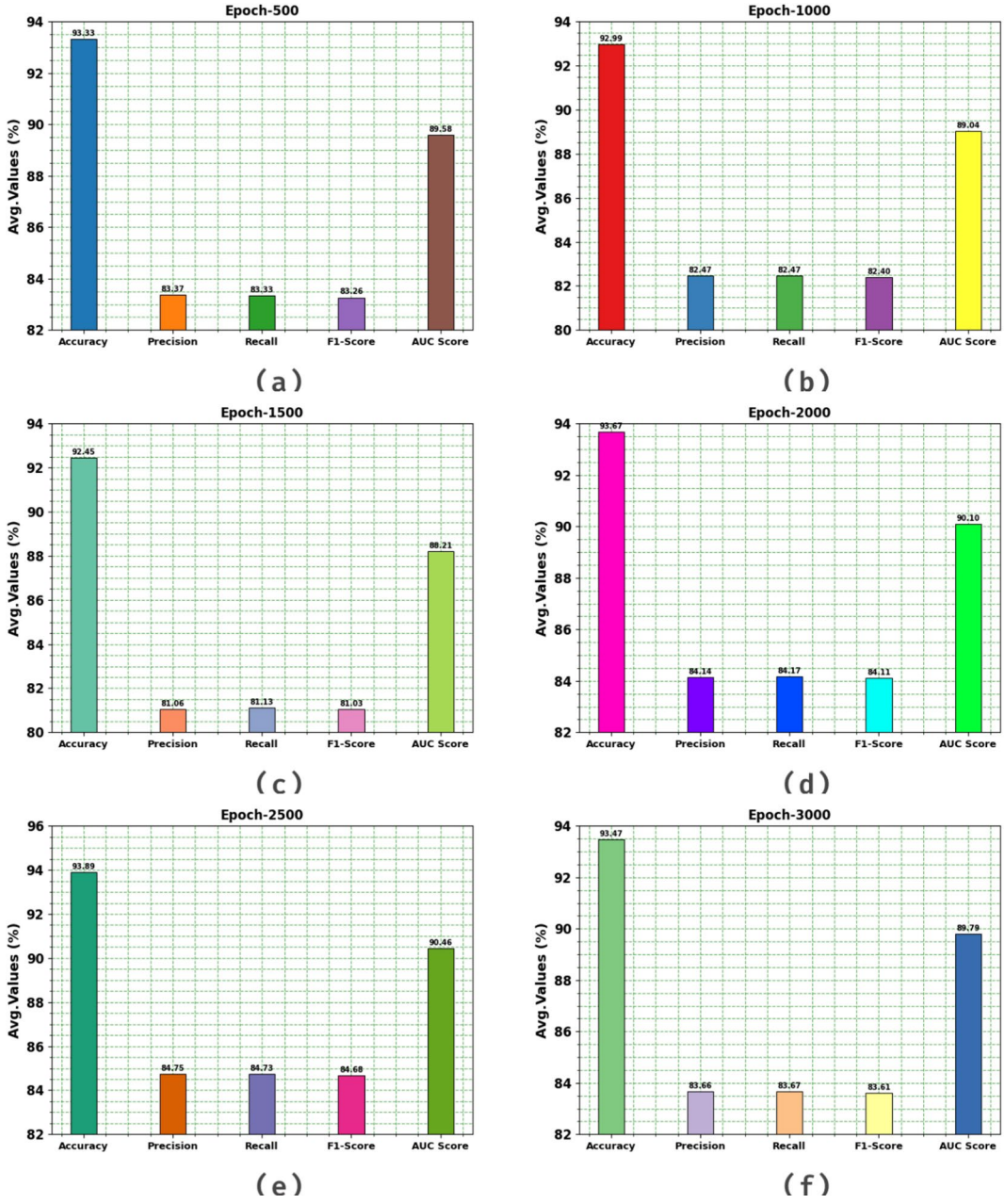

Fig. 7. Average of CVDTLM-AGRCC model (**a**–**f**) Epochs 500–3000.

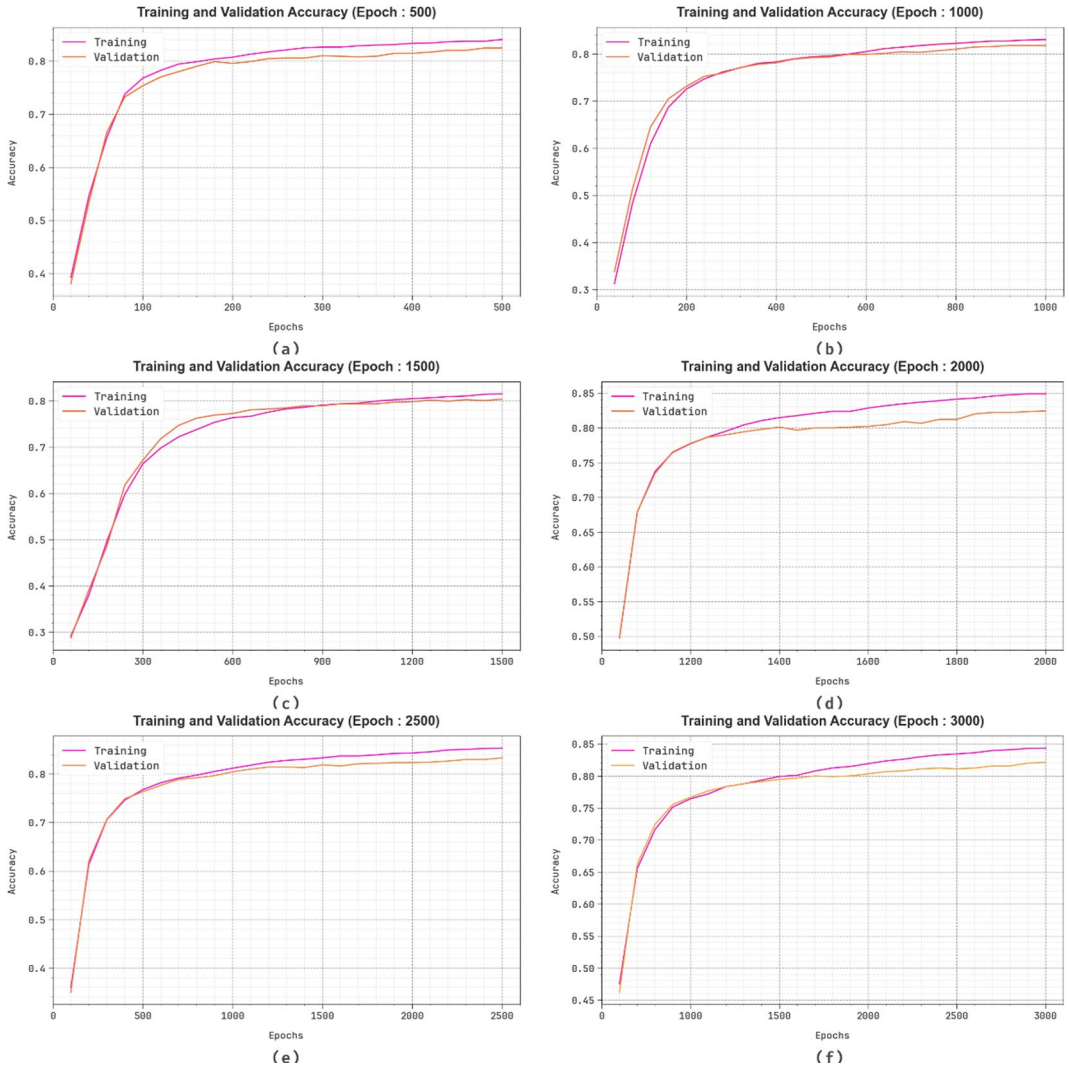

Fig. 8. $Accu_y$ curve of CVDTLM-AGRCC model (**a**–**f**) Epochs 500–3000.

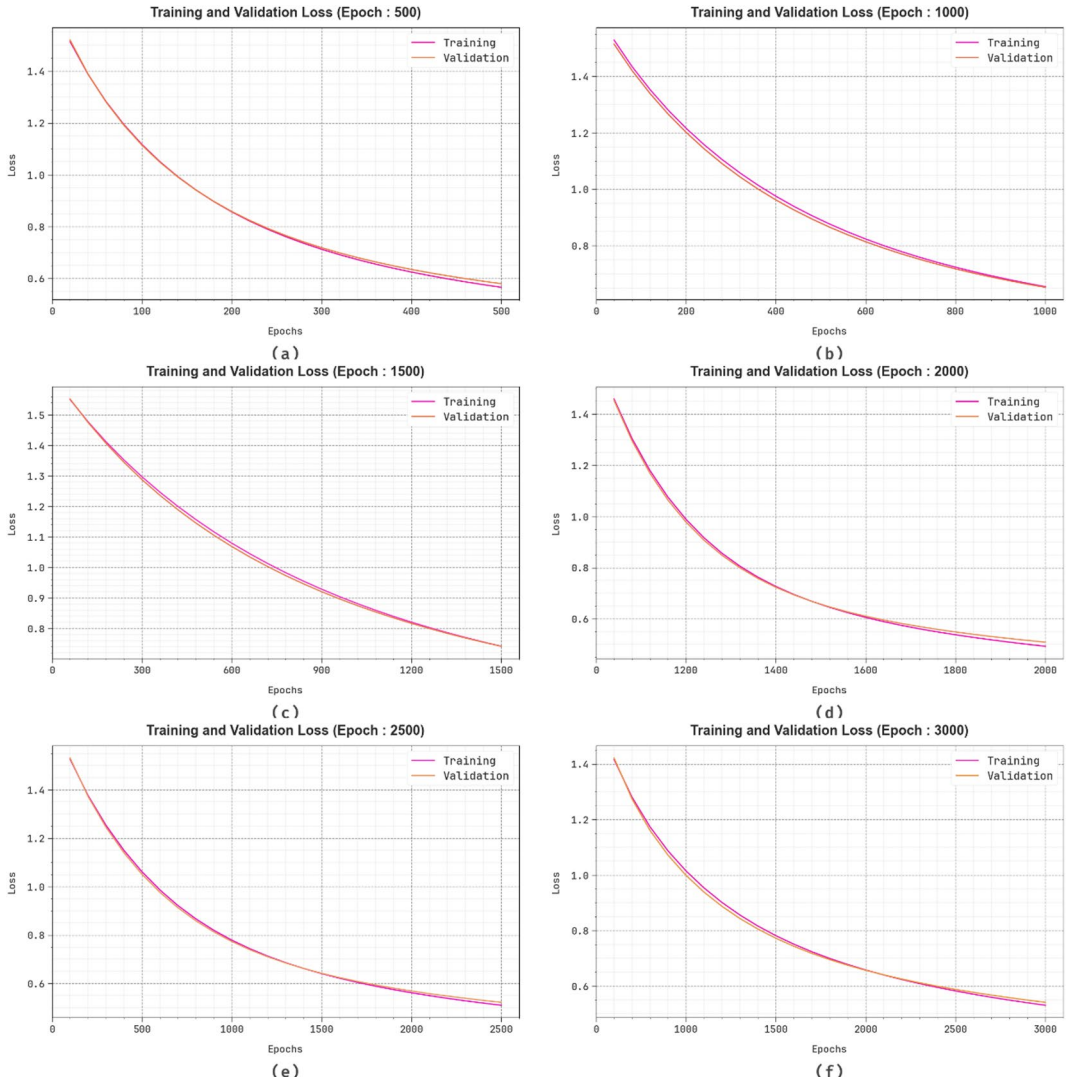

Fig. 9. Loss curve of CVDTLM-AGRCC model (**a**–**f**) Epochs 500–3000.

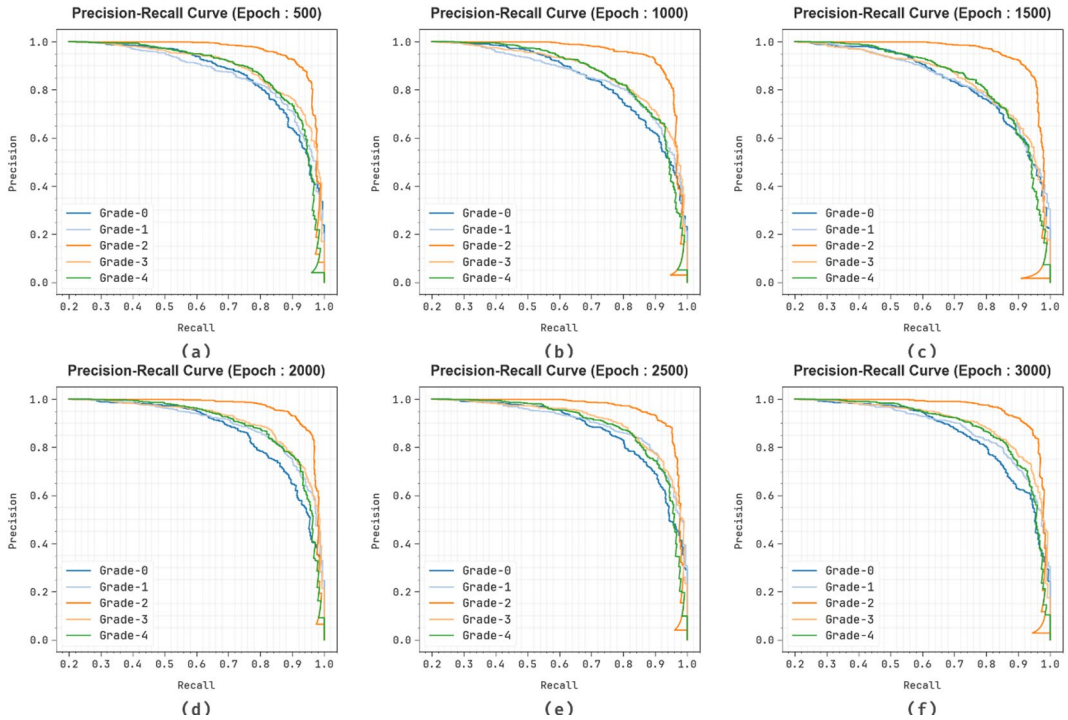

Fig. 10. PR curve of CVDTLM-AGRCC model (**a**–**f**) Epochs 500–3000.

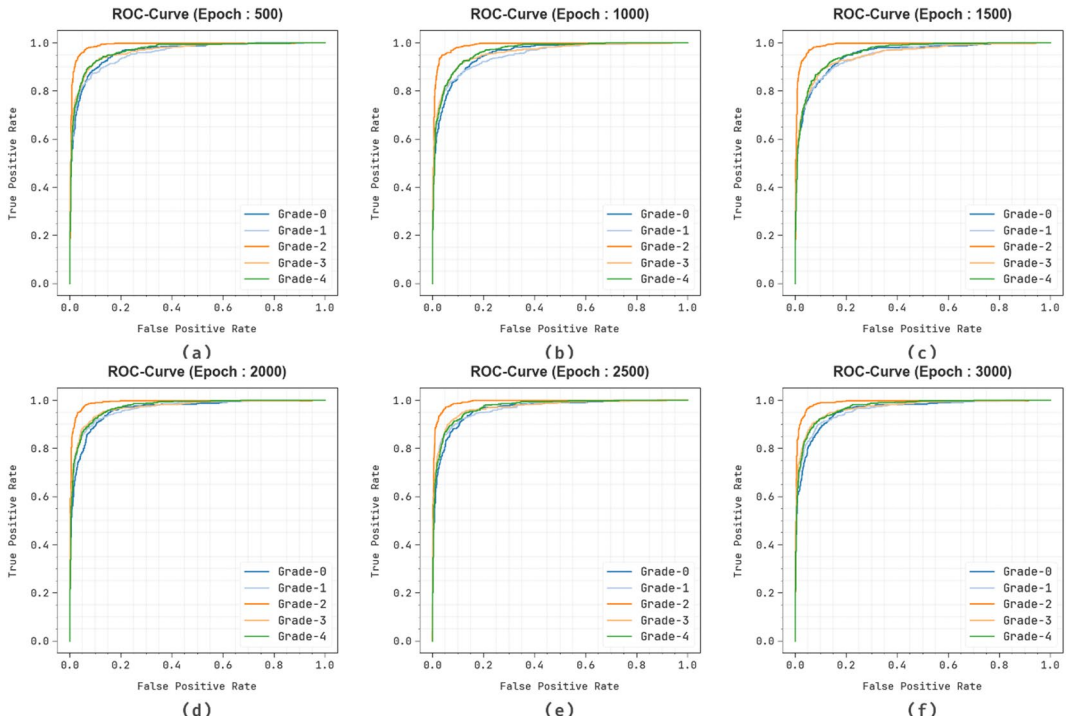

Fig. 11. ROC curve of CVDTLM-AGRCC model (**a**–**f**) Epochs 500–3000.

Approaches	$Accu_y$	$Prec_n$	$Reca_l$	$F1_{score}$
CVDTLM-AGRCC	93.89	84.75	84.73	84.68
XGBoost	86.59	77.17	84.17	80.62
RF	79.36	77.37	77.02	76.22
SHAP	78.15	72.17	74.31	71.01
ResNet-18 model	89.00	82.62	80.99	77.57
DLF-ACHKWI	92.00	82.71	79.72	78.73
SE_RESNET-50	90.11	75.88	79.59	82.88
REGNET-400	85.91	76.47	83.52	79.83
IncResV2 model	78.79	76.78	76.42	75.49
NASNet classifier	77.55	71.47	73.62	70.26
ShuffleNet model	80.18	78.97	75.07	75.79

Table 3. Comparative analysis of the CVDTLM-AGRCC technique with existing methods[19,26–28].

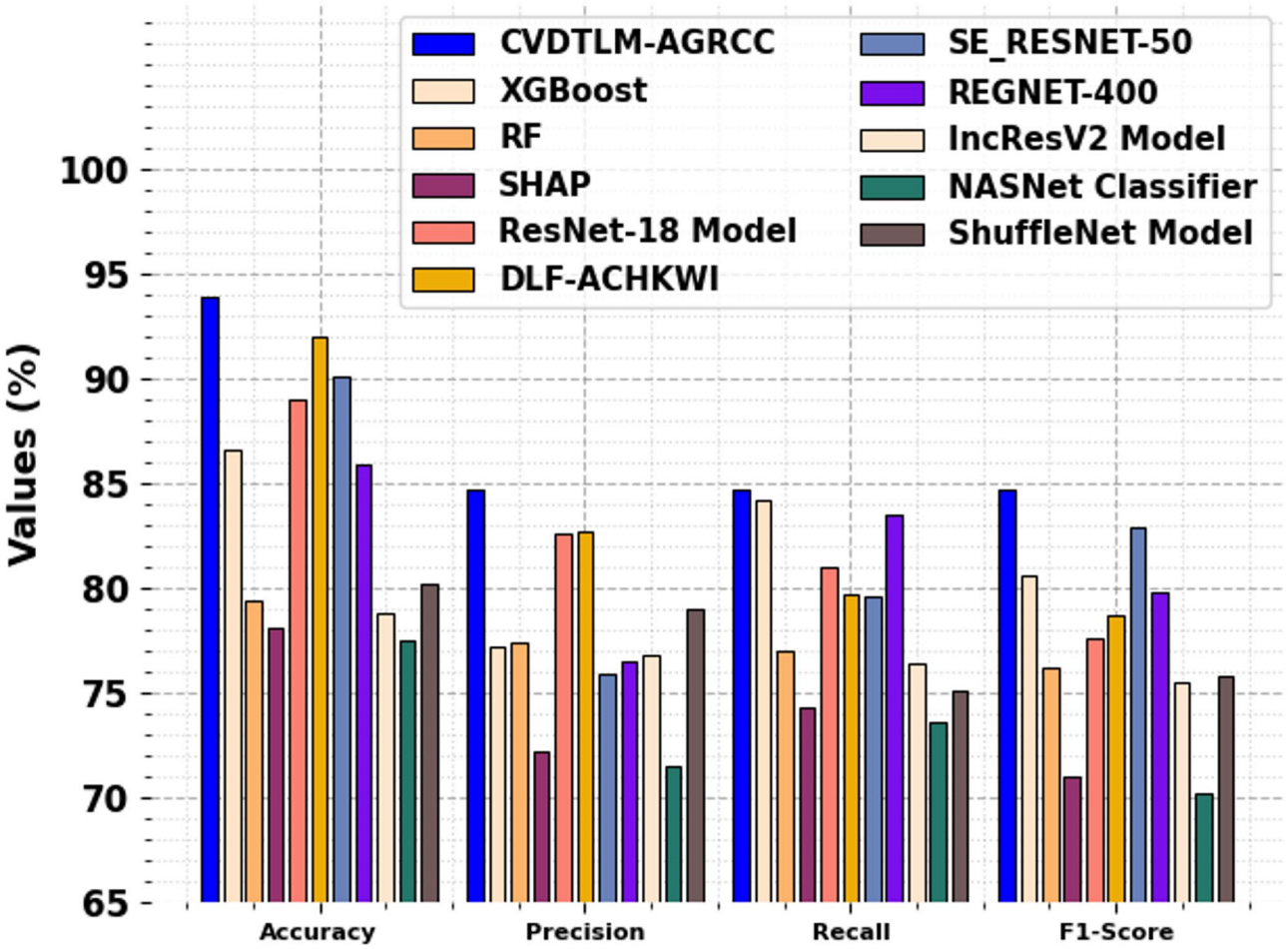

Fig. 12. Comparative analysis of the CVDTLM-AGRCC technique with existing methods.

Approaches	ET (s)
CVDTLM-AGRCC	3.18
XGBoost	5.90
RF	6.11
SHAP	8.00
ResNet-18 model	9.10
DLF-ACHKWI	9.89
SE_RESNET-50	7.55
REGNET-400	5.65
IncResV2 model	7.41
NASNet classifier	6.04
ShuffleNet model	9.31

Table 4. ET outcome of CVDTLM-AGRCC method with existing models.

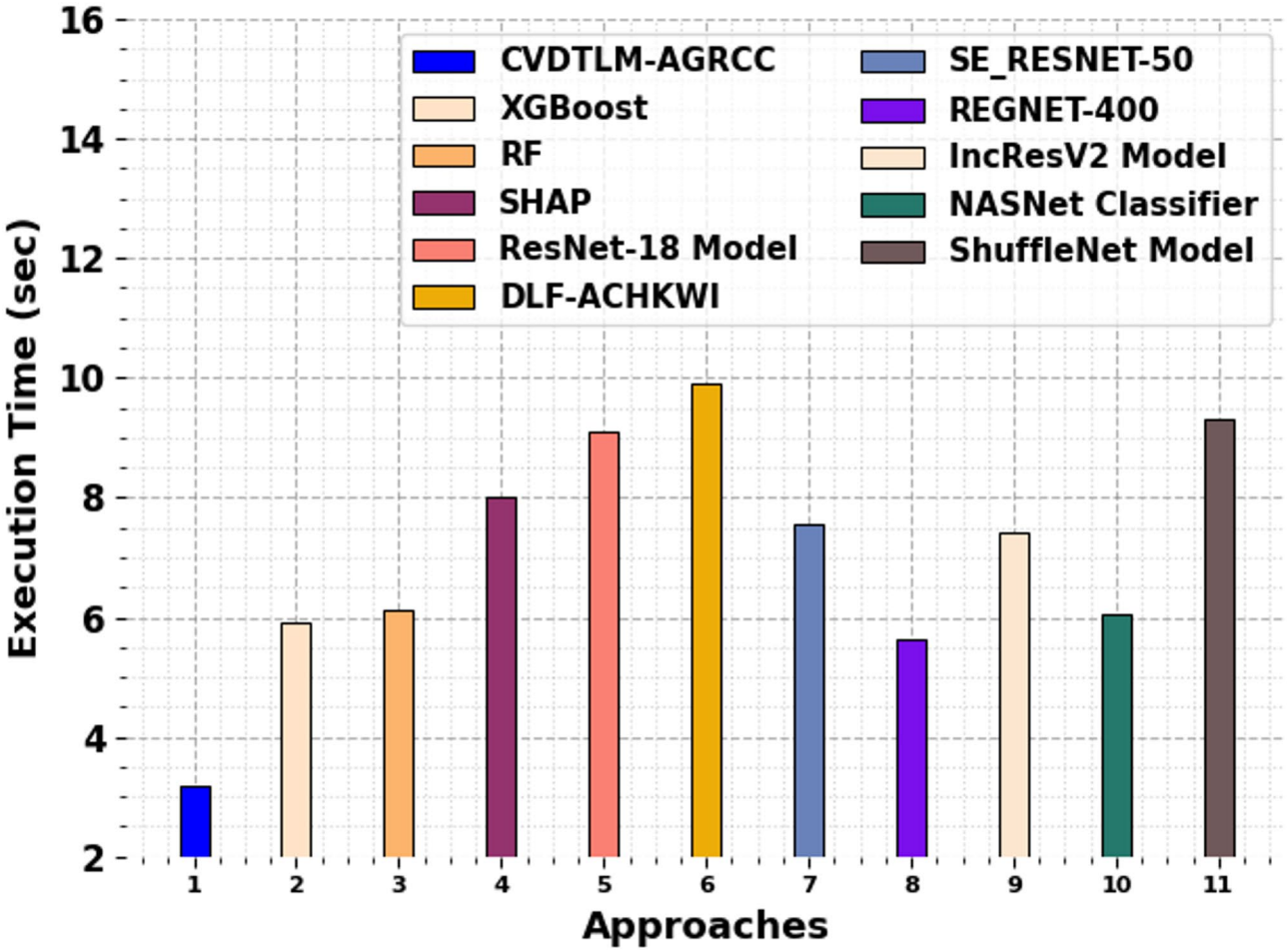

Fig. 13. ET outcome of CVDTLM-AGRCC method with existing models.

Data availability

The datasets used and/or analysed during the current study available from the corresponding author on reasonable request.

Received: 13 October 2024; Accepted: 11 September 2025
Published online: 15 October 2025

References

1. Yao, N. et al. A robust deep learning method with uncertainty estimation for the pathological classification of renal cell carcinoma based on CT images. *J. Imag. Inform. Med.* **38**(3), 1323–1333 (2024).
2. Wang, S. et al. A multi-model based on radiogenomics and deep learning techniques associated with histological grade and survival in clear cell renal cell carcinoma. *Insights Imag.* **14**(1), 207 (2023).
3. Gao, F. et al. Deep learning-based pathological prediction of lymph node metastasis for patient with renal cell carcinoma from primary whole slide images. *J. Transl. Med.* **22**(1), 568 (2024).
4. Pazhanirajan, S. Gazelle optimized visual geometry group network with resnet101 fostered oral squamous cell carcinoma detection. *J. Intell. Syst. Internet Things* **13**(2), 324–333 (2024).
5. Chen, S. et al. Artificial intelligence-based non-invasive tumor segmentation, grade stratification and prognosis prediction for clear-cell renal-cell carcinoma. *Prec. Clin. Med.* **6**(3), 1019 (2023).
6. Bai, Y. et al. Deep learning using contrast-enhanced ultrasound images to predict the nuclear grade of clear cell renal cell carcinoma. *World J. Urol.* **42**(1), 184 (2024).
7. Bolocan, V. O. et al. Convolutional neural network model for segmentation and classification of clear cell renal cell carcinoma based on multiphase CT images. *J. Imag.* **9**(12), 280 (2023).
8. Lu, C. et al. Multiphase comparative study for WHO/ISUP nuclear grading diagnostic model based on enhanced CT images of clear cell renal cell carcinoma. *Sci. Rep.* **14**(1), 12043 (2024).
9. Nie, P. et al. A preoperative CT-based deep learning radiomics model in predicting the stage, size, grade and necrosis score and outcome in localized clear cell renal cell carcinoma: A multicenter study. *Eur. J. Radiol.* **166**, 111018 (2023).
10. Dai, Y. et al. Grading clear cell renal cell carcinoma grade using diffusion relaxation correlated MR spectroscopic imaging. *J. Magn. Reson. Imaging* **59**(2), 699–710 (2024).
11. Kundu, S., Roy, N., Talukdar, R., Das, S., Mukhopadhyay, S. and Basu Mallik, B., 2024. RAF2Net: Automated grading of renal cell carcinoma utilizing attention-enhanced deep learning models through feature fusion. bioRxiv, pp. 2024-07.
12. Hao, F., Liu, X., Li, M. & Han, W. Accurate kidney pathological image classification method based on deep learning and multimodal fusion method with application to membranous nephropathy. *Life* **13**(2), 399 (2023).
13. Abu Haeyeh, Y., Ghazal, M., El-Baz, A. & Talaat, I. M. Development and evaluation of a novel deep-learning-based framework for the classification of renal histopathology images. *Bioengineering* **9**(9), 423 (2022).
14. Li, S. et al. Incremental value of automatically segmented perirenal adipose tissue for pathological grading of clear cell renal cell carcinoma: A multicenter cohort study. *Int. J. Surg.* **110**(7), 4221–4230 (2024).
15. Sun, X. et al. TGMIL: A hybrid multi-instance learning model based on the Transformer and the Graph Attention Network for whole-slide images classification of renal cell carcinoma. *Comput. Methods Programs Biomed.* **242**, 107789 (2023).
16. Mahootiha, M., Qadir, H. A., Bergsland, J. & Balasingham, I. Multimodal deep learning for personalized renal cell carcinoma prognosis: Integrating CT imaging and clinical data. *Comput. Methods Programs Biomed.* **244**, 107978 (2024).
17. Sukegawa, S. et al. Effectiveness of deep learning classifiers in histopathological diagnosis of oral squamous cell carcinoma by pathologists. *Sci. Rep.* **13**(1), 11676 (2023).
18. Patel, V. V., Yadav, A. R., Jain, P. & Cenkeramaddi, L. R. A systematic kidney tumor segmentation and classification framework using adaptive and attentive-based deep learning networks with improved crayfish optimization algorithm. *IEEE Access* **12**, 85635–83660 (2024).
19. Ranjitha, K. V. & Pushphavathi, T. P. Analysis on improved gaussian-wiener filtering technique and GLCM based feature extraction for breast cancer diagnosis. *Procedia Comput. Sci.* **235**, 2857–2866 (2024).
20. Duwe, G., Mercier, D., Kauth, V., Moench, K., Rajashekar, V., Junker, M., Dengel, A., Haferkamp, A. & Hoefner, T. Development of an artificial intelligence-generated, explainable treatment recommendation system for urothelial carcinoma and renal cell carcinoma to support multidisciplinary cancer conferences. medRxiv, pp. 2025-02 (2025).
21. Zhao, N. et al. Accurate classification of tunnel lining cracks using lightweight ShuffleNetV2-10-SE model with DCGAN-based data augmentation and transfer learning. *Appl. Sci.* **14**(10), 4142 (2024).
22. Aydin Atasoy, N. & Faris Abdulla Al Rahhawi, A. Examining the classification performance of pre-trained capsule networks on imbalanced bone marrow cell dataset. *Int. J. Imag. Syst. Technol.* **34**(3), e23067 (2024).
23. Guo, D., Sun, M., Wang, Q. & Zhang, J. Taxi demand method based on SCSSA-CNN-BiLSTM. *Sustainability* **16**(18), 7879 (2024).
24. Wei, Z., He, Z., Yang, F. & Sun, B. A method for optimizing terminal sliding mode controller parameters based on a multi-strategy improved crayfish algorithm. *Appl. Sci.* **14**(17), 8085 (2024).
25. https://drive.google.com/drive/folders/1BQZGKHKOUji9rDA5IVltlLnXLk7_Elic
26. Abdeltawab, H. A. et al. A deep learning framework for automated classification of histopathological kidney whole-slide images. *J. Pathol. Inform.* **13**, 100093 (2022).
27. Xu, L. et al. Deep learning using CT images to grade clear cell renal cell carcinoma: Development and validation of a prediction model. *Cancers* **14**(11), 2574 (2022).
28. Chanchal, A. K., Lal, S., Kumar, R., Kwak, J. T. & Kini, J. A novel dataset and efficient deep learning framework for automated grading of renal cell carcinoma from kidney histopathology images. *Sci. Rep.* **13**(1), 1–16 (2023).

Acknowledgments

The authors extend their appreciation to the Deanship of Research and Graduate Studies at King Khalid University for funding this work through Large Research Project under grant number RGP2/462/45. Princess Nourah bint Abdulrahman University Researchers Supporting Project number (PNURSP2025R203), Princess Nourah bint Abdulrahman University, Riyadh, Saudi Arabia. The authors extend their appreciation to the Deanship of Scientific Research at Northern Border University, Arar, KSA for funding this research work through the project number "NBU-FFR-2025-2248-07. The Authors would also like to thank Gulf University for Science and Technology (GUST) and the GUST Engineering and Applied Innovation Research Center (GEAR) for supporting this project under project code ISG-Case 143. The authors are thankful to the Deanship of Graduate Studies and Scientific Research at University of Bisha for supporting this work through the Fast-Track Research Support Program.

Author contributions

Mohammed Alghamdi: Conceptualization, methodology development, experiment, formal analysis, investigation, writing. Jamal Alsamri: Formal analysis, investigation, validation, visualization, writing. Khaled Mohamad Almustafa: Formal analysis, review and editing. Monir Abdullah : Methodology, investigation. Ahmad A. Alzahrani: Review and editing. Marwa Obayya: Discussion, review and editing. Abdulsamad Ebrahim Yahya: Conceptualization, methodology development, investigation, supervision, review and editing. All authors have read and agreed to the published version of the manuscript.

Funding
None.

Declarations

Competing interests
The authors declare no competing interests.

Ethics approval
This article contains no studies with human participants performed by any authors.

Consent to participate
Not applicable.

Informed consent
Not applicable.

Additional information
Correspondence and requests for materials should be addressed to A.E.Y.